Chapter 5

Observation of electrical and Magnetic properties of $Y_{1.5}Ca_{0.5}CoMnO_6$

5.1. Introduction

DP′s, having the formula $R_2MM'O_6$ (R indicates rare or alkaline earth elements and M and M′ are 3d/4d/5d group elements), have gained a lot of interest recently in research and technology. Double perovskite materials have a variety of fundamental and interesting physical characteristics, such as near-room temperature ferromagnetism, a significant magneto-dielectric effect, a massive MR%, a massive exchange bias effect, an exchange bias, Griffith phase, etc. [13,166–171]. As a response, these compounds have opened up new avenues for material research and extensive scope of possible applications, for example, spin filter junctions, spintronic devices, memory devices, magnetic sensors, etc. [61]. Due to amazing field-dependent magnetic behavior and outstanding physical features, double perovskite R_2CoMnO_6 materials containing magnetically active alkali earth (R) elements have received a lot of attention. The DP family has been the subject of extensive study, specifically La_2CoMnO_6 (LCMO) and La_2MnNiO_6 (LNMO). In both their ordered and disordered states, they display several extraordinary features [172]. There has been a lack of studies into DPs, including rare earth with lower cationic radii. The magnetic and physical nature of the DP system is altered by the size of the rare earth cations present in the system. The bond length and bond angle change significantly as the rare earth cationic size decreases. The resulting frustration in the octahedral-tilted structure modifies its magnetic and electrical properties.

In a magnetic field, $RCo_{0.5}Mn_{0.5}O_3$ (R = Y, Tb, Eu) shows a meta-stable nature, although having a lower spontaneous magnetization than LCMO [173]. However, Lu/Yb/Y doping at the La site (R_2CoMnO_6) will lead to (↑↑↓↓) E-type AFM order, which will break the symmetry inversion and arise to electrically polarized [174,175]. In particular, the magnetic ground states of the Y-based DP sample have received a lot of interest. The Y_2CoMnO_6 Magnetic ground state is still up for choice. A-site element substitution by cations of different ionic radii allows for interesting control of the magnetic, structural, and electric features of DPs. A-site element substitution by cations of different ionic radii allows for interesting control of the magnetic, structural, and electric features of DPs. As an example, in $EuMnO_3$, structural distortion arises when the Eu^{3+} ion is partially replaced by the Y^{3+} ion, which consequently impacts the material's magnetic and multi-ferroic features [176,177]. Given the opportunities in YCMO, we have conducted both an experimental and a first-principles study into partially Ca-substituted YCMO. The 3d-4f exchange interaction has a greater effect on influencing the magnetic order in the ground state.

5.2. Experimental detail

The double Perovskite sample YCCMO25 was synthesized in an aluminum crucible by solid state route using a muffle furnace in the air. The component materials Y_2O_3, Cao, CoO, and

Mn_2O_3 were utilized in a stoichiometric mixture (highly pure form of 99.99%), ground in mortar for about 60 minutes, and calcinated at a temperature of 1000 °C for 24 h. For proper calcination, the heating and cooling rates are 300 °C /h. After cooling, reground the sample for 40 minutes and again heated to 1080 °C for 30 hours. This calcination process was taken at 1150 °C and 1200 °C with an intermediate regrind sample. After calcination, we pressed powder into a circular pellet with a radius of about 5 mm and a width of 2 to 3 mm. The interaction of pallets was done at 1360 °C for 45 hours with a gradual cooling at 30 °C /h to induce phase development in the sample. We measured the XRD of a sintered sample to determine its structure.

5.3. Result and discussion

5.3.1. Structure study

Double perovskite preferred crystal structure dependency on the cationic charge, size, and A/B radius ratio, which are determined by the tolerance factor. The Goldschmidt tolerance factor for A-site $A_{2-x}A'_xBB'O_6$ double perovskite, which can be calculated by the equation, can be used to determine a crystal's stability, [117]

$$t = \frac{\frac{(2-x)r_A+(x)r_{A'}}{2}+r_O}{\sqrt{2}\left(\frac{r_B+r_{B'}}{2}+r_O\right)} \tag{26}$$

Where ionic radii are represented by r and corresponding elements are indicated by subscripts. The estimated value of the tolerance factor of YCCMO25 is 0.77, indicating the monoclinic or orthorhombic structure of YCCMO25 [170].

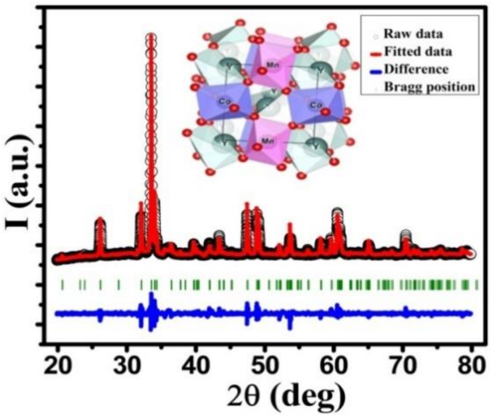

Figure 5.1: *The X-ray diffraction pattern using Rietveld refinement and the structure of YCCMO25 showing the tilted chains of (Co/Mn) O6 octahedral with an inset showing the 3D structure obtained using VESTA software.*

The XRD data, which was taken at ambient temperature, may be utilized to calculate crystalline phase, lattice constants, and estimated compositions of the YCCMO25 sample. Based on Rietveld refinements [178] of the sample's XRD data, it can be said that the crystallized sample was a single-phase monoclinic geometry having P21/n symmetry given in Fig 5.1. The monoclinic P21/n space group crystalline structure of YCCMO25 has a comparable volume space by using FULL-PROOF software [179]. The three-dimensional pattern of (Co/Mn) O_6 octahedral is visible in the structure of YCCMO25 as determined by the VESTA software.

5.3.2. X-ray Photoemission Spectroscopy study

The magnetic and electrical features strongly depend on the chemical electronic state of elements of the Double Perovskite system. Mixed valence states of the B and B' site cations are common in this system due to factors including charge compensation, synthesis condition, etc. [18]. The NIST-XPS database was utilized to determine the peak point and double separation of each element of the recorded data [180]**.** The surface elements Y, Ca, Co, Mn, and O were confirmed from the survey–scan of the sample from Fig 5.2 (a). The impurity of carbon (C_{1S}) peak was present in the spectrum at binding energy 284.24 eV. The peak of Y (3d) was fitted by XPS PEAK41 software is given in Fig 5.3(b). Core–level XPS spectrum of Y (3d) was split into two peaks, i.e. Y $3d_{3/2}$ (B.E. =159.21 eV) and Y $3d_{5/2}$ (B.E. = 157.01 eV) by spin-orbit coupling with doublet separation of 2 eV. From the fitting of Y (3d), it was confirmed that Y^{3+} exists. There was no satellite peak in the Y (3d) XPS spectrum. These two peaks were obtained because of the occupancy of the Y 4d state into $4d_0$ and $4d_1$. Fig 5.2(c) shows the core–level of the Ca (2p) XPS spectrum $2p_{3/2}$ and $2p_{1/2}$ of the system. The surface - scan of the sample showed that Ca exists in divalent states with $2p_{3/2}$ (346.7 eV) and $2p_{1/2}$ (350.2 eV) having a doublet partition of 3.5 eV for Ca^{2+} cations [181]. X-ray photoelectron spectra (XPS) of compounds with Co cations are given in the Fig 5.2(d). The core-level Co (2p) has its first intense peak around binding energy 779.7 eV corresponds to $2p_{3/2}$ and 795.4 eV corresponds to $2p_{1/2}$ which represents the Co^{3+} state [182]. The second intense peak of the Co^{2+} state around binding energy 797.1 eV ($2p_{1/2}$) and B.E. 781.1 eV ($2p_{3/2}$) with doublet separation B.E. (ΔE) 15.5 eV between Co ($2p_{1/2}$)and Co ($2p_{3/2}$) [182,183]. Additionally, there are two satellite peaks at binding energy 786.2 eV and 802.5 eV. This indicates that co-ions exist in a mixed oxidation state. It was shown that the energy gap (ΔE) between two levels due to spin-orbit coupling is dissimilar for divalent and trivalent ions, with $\Delta E = 15.5\text{-}16$ eV for Co^{2+} and $\Delta E = 15.0\text{-}15.2$ eV for Co^{3+}. This experiment determines that the binding energies of Co^{2+} and Co^{3+} are 15.5 and 15.1 eV, respectively. This result verifies the existence of Co^{2+} and Co^{3+} ions in our sample. The core–level Mn (2P) of sample YCCMO has two peaks Mn ($2p_{1/2}$) and Mn ($2p_{3/2}$) due to spin-orbit coupling. These peaks are de-convoluted into four successive peaks, P1, P2, P3, and P4, which together demonstrate the presence of Mn^{4+} ion in addition to Mn^{3+} ion, as seen in Fig 5.2(e). These peaks have doublet separation of binding energy 11.6 eV. The value of ΔE for Mn (2p) XPS spectrum in Mn_2O_3 is 11.6 eV and in MnO_2 is approximately 11.81 eV [184,185]. The XPS peak fitting of YCCMO clarifies that Mn (2p) has a mixed valence state. The first valence state Mn^{3+} has two peaks around binding energy 641.3 eV ($2p_{3/2}$) and 653.3 eV ($2p_{1/2}$). The second valence state Mn^{4+} has two peaks around binding energy 542.4 eV ($2p_{3/2}$) and 654.5 eV ($2p_{1/2}$) [186,187]**.** There is no satellite peak in this Mn-2p spectrum. The x-ray photoemission spectrum of Oxygen has shown two peaks given in the Fig 5.2(f) below. The core–level O1s have a strong peak at binding energy 528.4 eV due to the O^{2-} ion of lattice oxygen and a weak peak at B.E. 531.2 eV due to (O_2^-, O^-) absorption of oxygen [188–190].

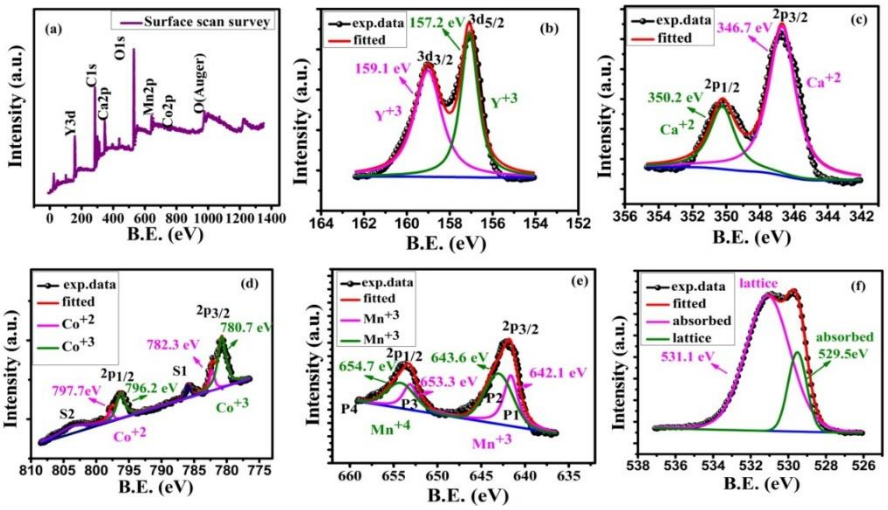

Figure 5.2: ***(a)–(f)*** *Surface scan & core-level XPS of different elements of YCCMO25.*

5.3.3. Resistivity measurement

The graph of electrical resistivity (ρ) vs. temperature (T), with resistance 12×10^9-1×10^9 Ohm, for sample YCCMO in the temperature range of 60—300 K, can be used to observe the insulating /semiconducting behavior of the material in Fig 5.3. Due to a higher resistance value, the limits of measurement are exceeded below the temperature of 55 K. Conduction bands in perovskite materials can be extremely narrow, which slows down electron speed. The lattice is polarized by the slowly moving electrons, and this polarization was carried along with the charge by the effect of the external electric field. It is well established that polaron regulates conductivity in most oxides. This phenomenon is possible in the context of thermally activated hopping. For the oxide sample, there is a different model to describe the charge transport behavior dependent on temperature as

$$\ln\rho \propto \frac{1}{n}$$

For n = 1, simple thermal activation model, and n = 4, Mott's Variable Range Hopping (VRH). The variation of resistivity at low temperatures can be fitted by the VRH model (60 -110 K). The VRH model can be used to explain the variation in resistivity for both systems below 200 K. This model assumes that only the states near to Fermi level whose energies lie within a narrow band are involved in conduction. Hopping resistances between neighbors become heavier than distant neighbors at lower temperatures. In VRH, charge transport is possible by thermally activated hopping between localized states given in the inset of Fig 5.3 below 110 K, the VRH mechanism is given by the equation [63,68,70]

$$\rho = \rho_0 exp(\frac{T_0}{T})^{1/4} \quad (27)$$

$$ln\rho = ln\rho_0 + ({T_0}^{1/4}).\,(T^{-1/4}) \quad (28)$$

Where T_0 is Mott's characteristic temperature, which governs the system's electrical transport properties and ρ_0 refers to the pre-factor. T_0 is given as,

$$T_0 = \frac{24\alpha^3}{\pi K_B N E_F} \quad (29)$$

Where (1/α) is the localization length of the wave function. N (E_F) is the density of the localized state near the Fermi level [67]. The numerical value of T_0 is calculated from the inclination of the fitted line with equation (29), T_0=1.3×10^9. The length of the localization (1/ α) is twice that of the Mn-Co bond length in numbers as well. At temperature T, the equation can be utilized to calculate the polaron activation energy (w).

$$W = \frac{1}{4}\left(K_B T_0^{1/4} T^{3/4} \right) \qquad (30)$$

With the most possible hopping distance

$$R = \left[\frac{9}{8\Pi\alpha K_B N E_F}\right]^{1/4} = \left[\frac{9T_0}{192\alpha^4}\right]^{1/4} \qquad (31)$$

For the systems at the Fermi level, the value of N (E_F) was determined to be approximately ∼ 10^{24} $eV^{-1}m^{-3}$, which is comparable to the value of a typical semiconductor oxide. Small Polaron Hopping (SPH) fitting is the best for resistivity as a temperature-dependent well at high temperatures (above 180 K) given in the inset of Fig 5.3. SPH fitting is given by the equation

$$\rho = \rho_0 T exp^{\frac{E_a}{TK_B}} \qquad (32)$$

The SPH fitting yielded the Polaron activation energy (E_a) as E_a = 18.89 meV. In response to heat, carriers of charge increase their drift mobility and hopping frequency, resulting in a short-range energy cycle [67,69,191].

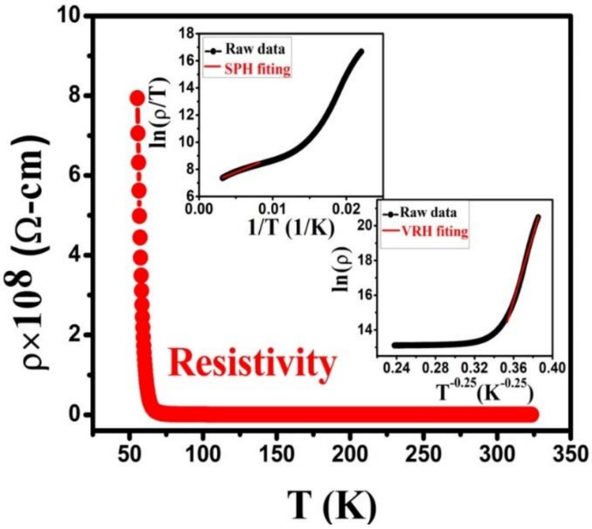

Figure 5.3: *The temperature variation resistivity of YCCMO25 with insets showing VRH and SPH fitting.*

5.3.4. Magnetic study

The magnetic features of the DP sample are known to be strongly affected by distortion and site disorder. Measurements of FC and ZFC magnetization M (T) as a function of temperature have been performed to elucidate the evolution of magnetic ground states in the presence of site disorder and distortion. The thermal variations (T) of the magnetization (M (T)) curve of Ca-doped YCMO under the impact of a 100 Oe DC magnetic field are depicted in Fig 5.4(a). The temperature dependence magnetization with zero fields 100 Oe is taken in warming conditions. Changes in magnetization are negligible down to 190 K, and after Tc, M (T) begins to increase as temperatures fall. The M-T curve demonstrates two magnetic transitions, with the significant ordering temperatures being derived using [dM_{ZFC}/dT] displayed in the inset of Fig 5.4(a). An abrupt change in magnetization was seen in both the FC and ZFC curves at the first transition T_{c1} = 180 K. This transition corresponds to the ferromagnetic transition that resulted from super-exchange interactions between Co^{2+}-O^{2-} -Mn^{4+} from the ordered sub-lattice. The magnetization value of the M_{ZFC} is maximum below Tc, near 45 K, and then begins to decrease at T_{c2} = 40 K, which demonstrates the non-zero polarization of magnetic ions behaving in an AFM-like behavior. This AFM phase transition may be due to the presence of ASD in our sample and the strong 3d-4f exchange interaction between the FM sub lattices of Co^{2+}/Mn^{4+} which is consistent with the Goodenough-Kanamori rules [3,148,192].

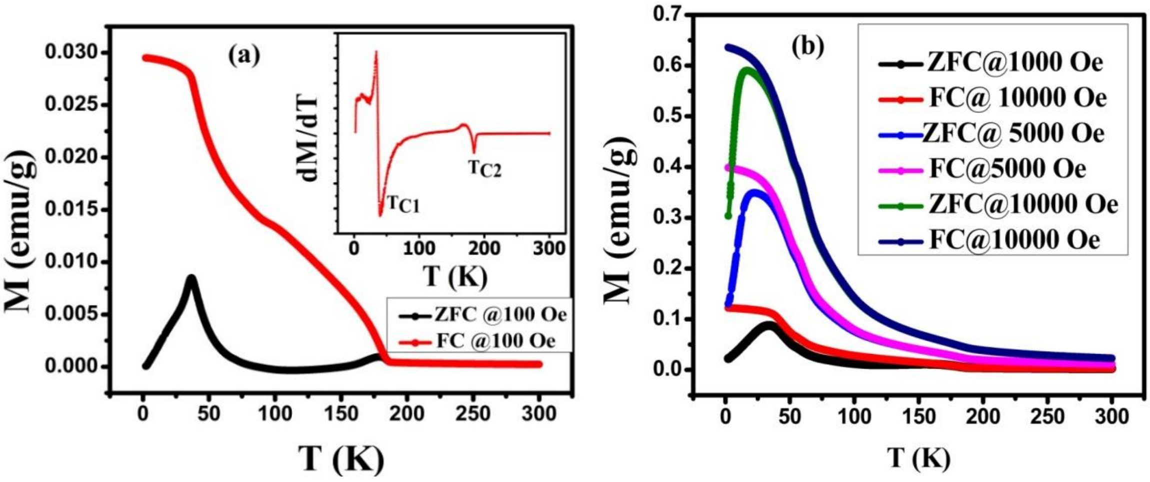

Figure5. 4: *(a) The temperature-dependent magnetization curves at two different applied ZFC and FC conditions. Inset: showing the derivative of the* M_{ZFC}*–T curve with inset showing the variation of* T_{C}*.(b) The ZFC/FC magnetization of YCCMO25 at 1 kOe, 5 kOe, and 10 kOe applied field.*

We are aware that the Antisite mismatch and the different valence states of Mn and Co components have significant effects on the magnetic features of DPs due to the altered B-O-B′ exchange interaction. A minor but negative value magnetization at an external magnetic field source of 100 Oe was seen in the ZFC data at lower temperatures. After ensuring that there were no residual fields, we performed the experiments again and got the same results, ruling out any probable instrumentation error. However, it is typical to observe negative magnetization at the lower field in a DP system of a similar nature. This is explained by the presence of tilted ferromagnetic (FM) domains or clusters and /or anti-parallel spins that are divided by the anti-phase perimeter, which is brought about by ASD [193]. Even at low temperatures, a field of 100 Oe is not strong enough to get the frozen spins lined up of all the clusters and domains. It could be an indication of the stabilization of the glassy state, the AFM state, or the low-temperature tilted spin state, which results in a negative residuum magnetization in the ZFC condition [134]. Below 40 K in the magnetic moment, the ZFC curve can also be seen to change. Upon application of a magnetic field at 100 Oe, this transition is visible as an apex in the M-T graph. The transition at 36 K may be brought on by spin freezing, the presence of an AFM component next to an FM component, or the presence of a glassy magnetic phase.

The temperature dependence magnetization with zero fields 1 kOe, 5 kOe, and 10 kOe has a temperature domain of 2- 300 K given in Fig 5.4(b). The useful data are taken in warming conditions. The FC and ZFC graph bifurcate, with the amplitude of the bifurcation increasing as we increase the magnetic field from 100 Oe to 10 kOe, and bifurcation is absent at the 40 kOe field. Transition temperature (Tc) also increases with increasing applied field. The bifurcation between FC and ZFC occurs at a temperature called the temperature of the freezing spin (T_f), which is consistent with the presence of a glass transition [76]. In the ZFC magnetization vs. temperature graph, obtaining a cusp near the temperature Ta will shift to a lower temperature as an increasingly higher magnetic field indicates the presence of the AFM phase or anti-phase region in the sample. At the temperature of Ta's cusp, the energy carried by the applied field and the energy of anisotropy are roughly equal, which explains the temperature of Ta's cusp nature. In the M-T graph, the presence of bifurcation among ZFC and FC is usually present in the FM system. The reduction of magnetic anisotropy energy leads to the initial bifurcation, which appeared at the lower temperature side with a stronger magnetic field.

5.3.5. DC Susceptibility

The temperature-dependent inverse of susceptibility is depicted in Fig 5.5(a) to demonstrate the behavior of magnetization in higher-temperature regions (i.e. in the PM state) and the inset of Fig 5.5(b) shows a closer view.

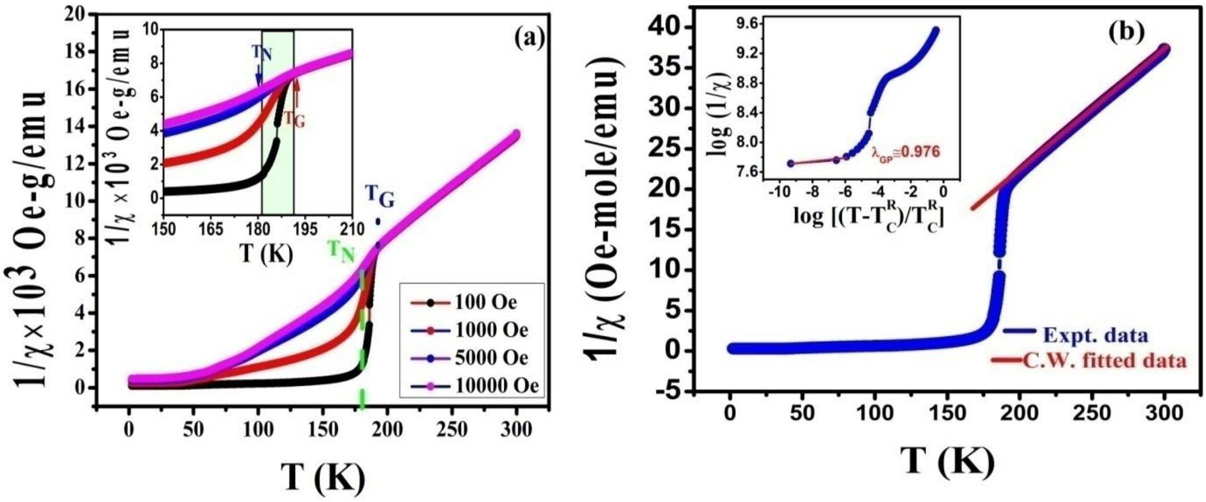

Figure5. 5: *(a) The temperature-dependent inverse susceptibility curves at different fields. Inset: shows a closer view of the down-turn behavior. (b) Presents 'Curie–Weiss fit to the 1/χ versus T plot. Inset: depicts the power law fitting to the log-log plot of '*χ^{-1} *versus ((*$\mathrm{T} - \frac{\mathrm{T_C^R}}{\mathrm{T_C^R}}$*))'.*

Since the curve deviates from linearity above Tc, the standard Curie-Weiss law has some deviation in the PM region. We used Curie-Weiss fitting to the "inverse susceptibility (1/χ) vs. T" graphs to determine the effective paramagnetic moment (μ_{eff}) and the Curie-Weiss temperature (T_{CW}) for the sample. The classic Curie-Weiss (CW) model, is given as

$$\frac{1}{\chi} = \frac{M}{H} = \frac{3K_B}{U_{eff}^2}(T - T_{CW}) \qquad (33)$$

C-W is used to match the temperature fluctuation of the χ^{-1} graph in the increased temperature domain. The results of the fitting curve were $\mu_{eff} = 5.43\ \mu_B$ and $T_{CW} = +\ 55$ K. The positive quantity of T_{CW} shows the supremacy of ferromagnetic couplings in the system given in Fig 5.5(b). Additionally, the significant discrepancy between the transition temperature (T_C) and T_{CW} indicates spin frustration is present in the system. The DC inverse susceptibility curve of YCCMO25 has been seen to exhibit a linear nature above 200 K, demonstrating a pure PM state. Just below 190 K (T_{GP}), it has been seen that the χ^{-1}(T) exhibits a downward departure from the C-W line like to PCMO. Rare-earth elements typically produce numerous magnetic interactions in the system, leading to heterogeneous magnetic ground states, such as clustered or phase-separated states like the Griffith phase [1,35,194].

To examine the GP, we investigated the temperature change of $1/\chi$ in several application fields. The figure clearly shows that at temperatures $T > T_C$, the lower-field $1/\chi$ curves exhibit a definite downturn tendency. The GP forms in the vicinity $T_{C1} > T > T_{GP}$ below Griffith's temperature (T_{GP} = 190 K), where the sample shows an anomalous magnetic phase as a result of the production of short-range Ferromagnetic clusters of various sizes in the PM region. The down-turn characteristic is eliminated when the larger fields finally increase the surrounding PM moments and obscure the FM cluster contribution [195]. Due to the development of FM clusters, the susceptibility within the Griffith Phase region, i.e.$T_C < T < T_{GP}$, becomes an anomalous magnetic field function and obeys the Power rule defined by

$$\chi^{-1}(T)\ \alpha\ (T- T_C^R)^{1-\lambda},\ \ (0<\lambda< 1). \tag{34}$$

Here, T_C^R is the lowered long-term ordering temperature as a result of random non-magnetic dilution, and λ is a measure of departure from CW behavior [1,34,37]. Though choosing T_C^R = T_{CW} would result in $\lambda \sim 0$ at the PM area, in this situation, due to the occurrence of AFM/FM interactions, T_{CW} sits significantly lower Ferromagnetic ordering temperature. It is important to choose the T_C^R value in such a manner that equation (34) produces a result that λ is almost zero in the PM zone when $T > T_{GP}$. As a result, the T_C^R value will be almost identical to the T_{CW} temperature that was established via the CW formula fitting in the PM zone of high temperature. The calculated value of λ =0.97 from the GP's linear fit area indicates that the sample contains GP for YCCMO25 given in the inset of Fig 5.5(b).

5.3.6. Field–dependent Magnetization

At constant temperature, magnetization M (H) experiments have been carried out towards a field of 5 T at temperatures 2, 60, 170, and 300 K, given in Fig 5.6 respectively, in ZFC mode, to clarify the magnetic characteristics of YCCMO25 with the modification of the applied field. Fig 5.6 inset depicts the connection of T with H. At 2 K, the M (H) loop exhibits an FM-like nature with a magnetic coercivity of 12.73 μ_B /f.u. and a significant coercive field (H_C) of 7.175 kOe. At 300 K, the M (H) graph is an exact linear line that acts like a pure PM and is free of other magnetic impurities. The graph shows that when the temperature drops, magnetization values rise. The magnetization is unsaturated even when H = 5 T, as shown by the hysteresis loops observed at temperatures of 2, 60, 170, and 300 K. This property is easily apparent due to the presence of rare-earth sub-lattice in this substance. This unsaturated magnetization is due to the 3d-4f exchange interaction and ASD in the sample. We have therefore estimated the saturation magnetization value from the virgin M(H) graph displayed in the inset of Fig 5.6 obtained at 2 K by fitting the higher field region (H >20 kOe) using the given formula [196].

$$\mathrm{M\ (H)} = M_S(1-\frac{P}{H}-\frac{Q}{H^2})+rH \tag{35}$$

Where r represents the high-field differential susceptibility of the system, P is a structural defect and nonmagnetic inclusion of local magnetic moments and Q is related to magneto-crystalline anisotropy. The obtained value of M_S is 3.1 μ_B/f.u. At a field of 5 T, which is lower than the 6.0 μ_B/f.u. Theoretical estimate for fully polarized Co^{2+}-O^{2-}-Mn^{4+}. However, compared to its crystalline, where saturation was discovered at 60 T, the Lu_2CoMnO_6, a single crystalline sample has attained saturation magnetization at moderate fields (3 T). This suggests that magnetic pinning forces have a major effect on magnetism in polycrystalline samples. The figure shows that our sample has a high coercivity even at extremely cold temperatures. This can be explained by the magneto crystalline anisotropy of the sub-lattices and the setting of the FM domain boundary because of ASD defects [196]. At higher temperatures, the thermoenergy dampens the energy of the magneto-crystalline anisotropy, the domain boundary begins to move, and the coercivity drops [197]. As a consequence of ASD, the YCCMO25 molecule exhibits several different magnetic phases; therefore, meta-magnetic transitions are to be expected in the hysteresis curves. It has been established that $RCo_{1-x}Mn_xO3$ (R =Nd, Y, Eu,) shows this nature [100]. In the parent system Y_2CoMnO_6, there is a 'step-like' behavior at low temperatures below 5 K, as we increase the temperature this step will disappear. This step also depends on the applied field sweep rate. At 5 K the magnetic field increases as FC 10 kOe then the step will be removed. In the sample Y_2CoMnO_6, the exchange bias is less than 500 Oe at the external field of 10 kOe. It is discovered that the virgin loop is outside of the body of the envelope. Steps are lacking in magnetic field reverse-sweep. In our system, we doped Ca at the Y site by 25%, we get there is no step in the M-H curve. In the M-H graph, the magnetization has not saturated at 2 K on applied field 5 T. The magnetic hysteresis loop decreases as temperature increases and its loop will disappear at 170 K. The parent sample Y_2CoMnO_6 has exchange bias H_{EB} = 500 Oe while doping Ca in the system H_{EB} reduced to 200 Oe [198].

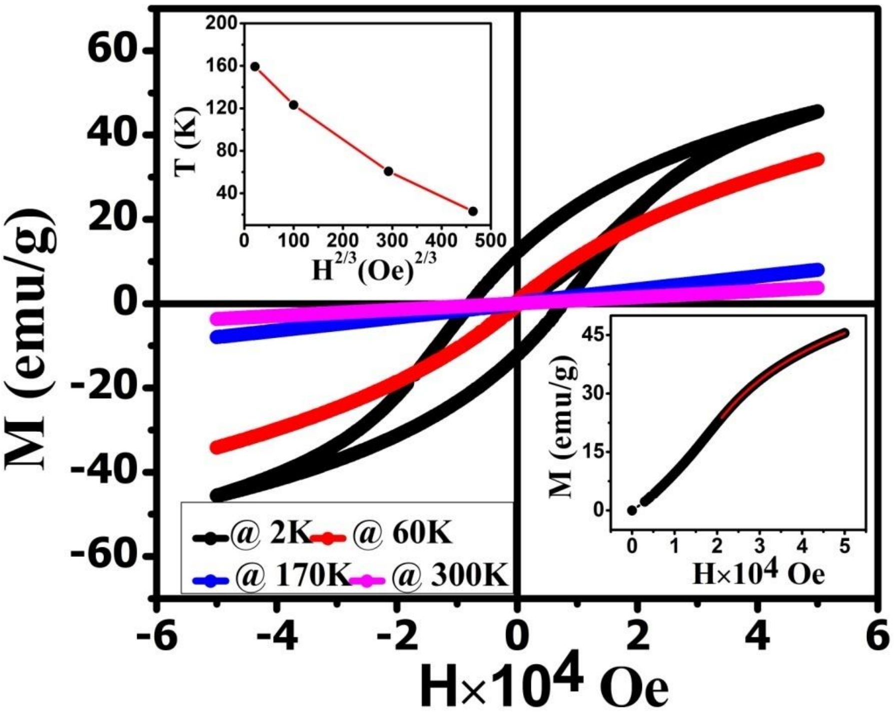

Figure 5.6: *The isothermal magnetizations vs. magnetic field of YCCMO25 at different temperatures. The upper Inset shows the variation of Ta with H and the lower inset shows an M-H virgin curve.*

5.4. Summary

In conclusion, the impact of ASD on the magnetic and physical characteristics of Ca-doped YCMO has been studied. Refining the structure of the chemical YCCMO25 has shown that its main phase has a monoclinic phase and space group $P2_1/n$. XPS investigation revealed the existence of Co and Mn ions in mixed-valence states due to Ca doping. The temperature dependence of the resistivity measurement reveals its semiconducting behavior, which is typified by range hopping and spin-polaron hopping. Magnetic measurements allow us to ascertain that the T_C and T_{CW} of a double perovskite sample are 180 K and 56.4 K, respectively. DC susceptibility analysis shows there is a Griffith-like cluster phase presence in the paramagnetic region above the magnetic ordering temperature. Isothermal field-dependent magnetization shows no sign of a meta-magnetic phase at 2 K, because of Ca ion doped at the Y site decreases magnetic interaction between transition metal ions.